An Excess-Calcium-Binding-Site Model Predicts Neurotransmitter Release at the Neuromuscular Junction

Markus Dittrich,[†‡§*] John M. Pattillo,[‡] J. Darwin King,[‡] Soyoun Cho,[‡] Joel R. Stiles,[†‡§] and Stephen D. Meriney[‡]
[†]National Resource for Biomedical Supercomputing, Pittsburgh Supercomputing Center, Carnegie Mellon University, Pittsburgh, Pennsylvania; [‡]Department of Neuroscience and [§]Department of Computational and Systems Biology, University of Pittsburgh, Pittsburgh, Pennsylvania

ABSTRACT Despite decades of intense experimental studies, we still lack a detailed understanding of synaptic function. Fortunately, using computational approaches, we can obtain important new insights into the inner workings of these important neural systems. Here, we report the development of a spatially realistic computational model of an entire frog active zone in which we constrained model parameters with experimental data, and then used Monte Carlo simulation methods to predict the Ca^{2+}-binding stoichiometry and dynamics that underlie neurotransmitter release. Our model reveals that 20–40 independent Ca^{2+}-binding sites on synaptic vesicles, only a fraction of which need to bind Ca^{2+} to trigger fusion, are sufficient to predict physiological release. Our *excess*-Ca^{2+}-binding-site model has many functional advantages, agrees with recent data on synaptotagmin copy number, and is the first (to our knowledge) to link detailed physiological observations with the molecular machinery of Ca^{2+}-triggered exocytosis. In addition, our model provides detailed microscopic insight into the underlying Ca^{2+} dynamics during synapse activation.

INTRODUCTION

Synapses, which have been studied intensely for many decades, are at the core of neural function and disease, and their proper operation underlies virtually all somatic and cognitive processes. Unfortunately, due to the difficulty of studying synapses in microscopic detail using experimental approaches, we currently lack a precise molecular and mechanistic understanding of synaptic function, in particular excitation-secretion coupling.

Here, we describe the development of a quantitative and predictive computational model of synaptic function at the neuromuscular junction (NMJ) that provides molecular-level resolution. Our model uses accurate Monte Carlo simulations and leverages extensive experimental data to constrain system parameters. Specifically, our model integrates data for synaptic physiology, structure, and molecular biology, and includes voltage-gated Ca^{2+} channels (VGCCs), a detailed 3D active zone (AZ) ultrastructure complete with synaptic vesicles, and quantitative stochastic simulation of Ca^{2+} influx, diffusion, and binding.

With this model in hand, we could then suggest and test new hypotheses. In particular, we examined the relationship of quantitative synaptotagmin-vesicle stoichiometry and Ca^{2+} binding to the physiological properties of neurotransmitter release. We know that synaptic vesicle release depends roughly on the fourth power of extracellular Ca^{2+} concentration (the calcium-release relationship (CRR) (1)). Hence, most physiological models to date have assumed four to five cooperative binding sites to trigger vesicle release (2–6) or elaborations thereof (7,8). However, recent biochemical data strongly suggest that vesicular synaptotagmin molecules bind Ca^{2+} to trigger release, that synaptotagmin C2A and C2B domains have a total of five Ca^{2+}-binding sites (9), and that each vesicle may have up to 15 copies of synaptotagmin (10,11). In addition, it was suggested that Ca^{2+}-bound synaptotagmin C2 domains interact with the presynaptic membrane (12), and that three to eight SNARE complexes initiate fusion of docked vesicles (9,13).

With the help of our model, we were able to show that multiple independent synaptotagmin Ca^{2+}-binding sites (20–40, corresponding to four to eight synaptotagmin molecules), only a subset of which had to bind Ca^{2+} to trigger release (five or six sites), are sufficient to predict physiological synaptic vesicle release without assuming any ad hoc site cooperativity. Our excess-Ca^{2+}-binding-site model agreed well with available data and reproduced the measured average number of released vesicles, the fourth-order CRR, and the narrow distribution of release latencies. Our model provides the first (to our knowledge) integration of existing molecular and physiological data to predict quantitative mechanisms of transmitter release. In the future, we plan to use our model to probe mechanisms of synaptic plasticity, neurological diseases, effects of drug treatments, and AZ structure-function relationships.

Submitted February 19, 2013, and accepted for publication May 6, 2013.

*Correspondence: dittrich@psc.edu

Joel R. Stiles is deceased.

John M. Pattillo's present address is Macon State College, Macon, Georgia.

J. Darwin King's present address is Renal-Electrolyte Division, University of Pittsburgh, Pittsburgh, Pennsylvania.

Soyoun Cho's present address is the Vollum Institute, Oregon Health & Science University, Portland, Oregon.

Editor: Michael Stern.

0006-3495/13/06/2751/13 $2.00

http://dx.doi.org/10.1016/j.bpj.2013.05.023

MATERIALS AND METHODS

Model geometry

Spatially realistic model geometries for MCell simulations can be obtained in several ways, such as by reconstruction from electron microscopy imagery (14) or by in silico methods using computer-aided design or three-dimensional (3D) content creation software (15). The latter is a powerful new approach for modeling complex biological structures that allows for rapid creation of model geometries and thus complements traditional reconstructions from electron microscopy. We used Blender (16) to create our model's 3D mesh geometry in silico according to dimensions based on published averages (17,18) (see Fig. 1). Our model included 26 synaptic vesicles of 50 nm diameter arranged in two double rows. We marked triangular mesh tiles on the bottom of each synaptic vesicle as putative Ca^{2+}-sensor sites. Similarly, mesh tiles in the trough between vesicles were marked as putative VGCC sites at locations suggested by published estimates (17–19). These marked tiles could then be populated with Ca^{2+}-sensor sites or VGCCs as needed within MCell's Model Description Language (MDL). From Blender, meshes were exported directly into MDL.

MCell simulations and algorithms

All simulations were carried out with MCell version 3.1 (rev. 788) with a custom binary reaction data output format to facilitate data handling. For each simulation condition (different numbers of Ca^{2+}-sensor sites on vesicles, varying extracellular Ca^{2+} concentration, etc.), we averaged the results over 10,000 separate MCell runs obtained via different random number seeds. During each run we tracked the Ca^{2+} ions emerging from individual VGCCs, their binding to Ca^{2+} buffer, and their binding to Ca^{2+}-sensor sites on vesicles. Ca^{2+} ions that encountered the edges of our model geometry were removed from the simulation to mimic their disappearance into the adjacent presynaptic space. We used programs written in C++, Python, Lua, and Bash to analyze the data. All simulations were run on the Salk machine at the Pittsburgh Supercomputing Center, an SGI Altix 4700 shared-memory NUMA system with 144 Itanium2 processors, cmist, an eight-core Intel Xeon E5472 machine, or a local desktop with an Intel i7-980X CPU.

We previously described MCell's simulation algorithms in detail (20,21). In brief, in an MCell model, the membranes of cells and organelles are represented by triangulated surface meshes. Brownian motion of diffusing volume and surface molecules is simulated using optimized grid-free Brownian dynamics random walk algorithms (21). Due to the inherently small length scales present in our model (e.g., distances between VGCCs and synaptic vesicles or between vesicles and the presynaptic membrane), we used a small simulation time step of 10 ns and corresponding short diffusion step lengths to allow for accurate spatial sampling (22).

Simulation of VGCCs and Ca^{2+} influx

VGCCs in our model opened and closed according to a time-dependent action potential waveform (Fig. 2 A) and were modeled via a four-state kinetic scheme (three closed states and one open state; see Table 1 and *inset* in Fig. 2 *A*). The rate constants between states were voltage dependent with the following parameters (23):

$$\alpha = 0.06e^{(V_m+24)/14.5}$$

$$\beta = \frac{1.7}{e^{(V_m+34)/16.9}+1}.$$

Here, $V_m(t)$ is the time-dependent membrane voltage corresponding to the action potential waveform shown in Fig. 2 *A*. The time-dependent rate constants α and β were precomputed and stored in separate text files that were then read by MCell at the beginning of each simulation. Because the extracellular Ca^{2+} concentration, $[Ca^{2+}]_{ext}$, remains approximately constant during an action potential, we approximated Ca^{2+} flux through open

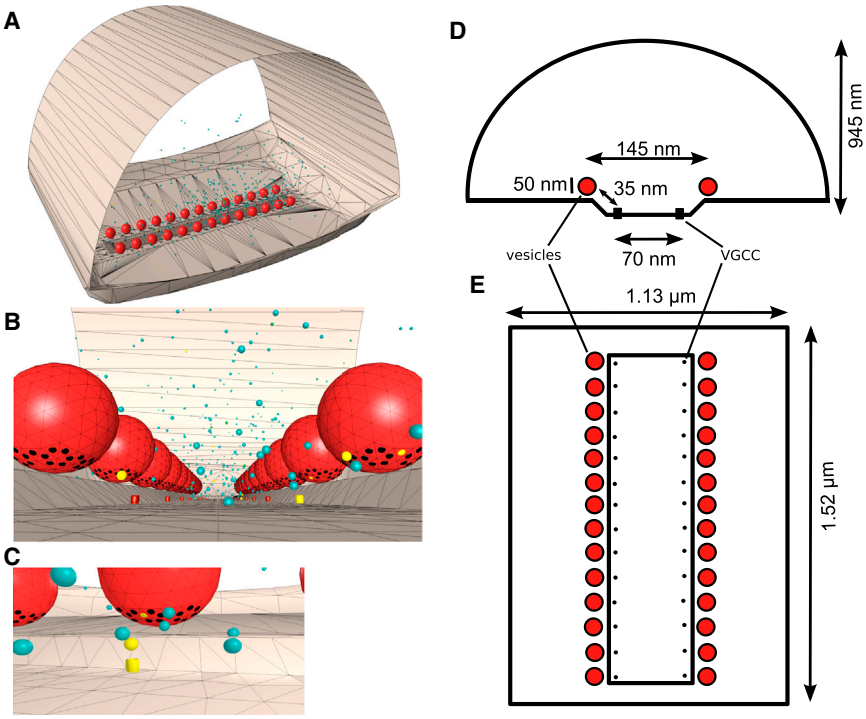

FIGURE 1 Overview of the frog NMJ model. (*A*) Rendered simulation snapshot of the complete AZ model. Visible are the two double rows of synaptic vesicles (*large red spheres*) as well as diffusing free and buffer-bound Ca^{2+} ions (*small colored spheres*). For visual clarity, unbound buffer sites are not shown. (*B* and *C*) Close-ups of synaptic vesicles, revealing the Ca^{2+}-sensor sites at their bottom (the 40-sensor model is shown). The cylindrical glyphs directly in front of synaptic vesicles represent closed or open VGCCs (*red*, closed; *yellow*, open). Open VGCCs release Ca^{2+} ions (*yellow spheres*) into the presynaptic space, which can bind to endogenous buffer sites (*cyan spheres*; only Ca^{2+}-bound buffer sites are shown) or sensor sites on synaptic vesicles. Unbound and bound Ca^{2+}-sensor sites on vesicles are colored black and yellow, respectively. (*D* and *E*) Important model dimensions (drawings are not to scale).

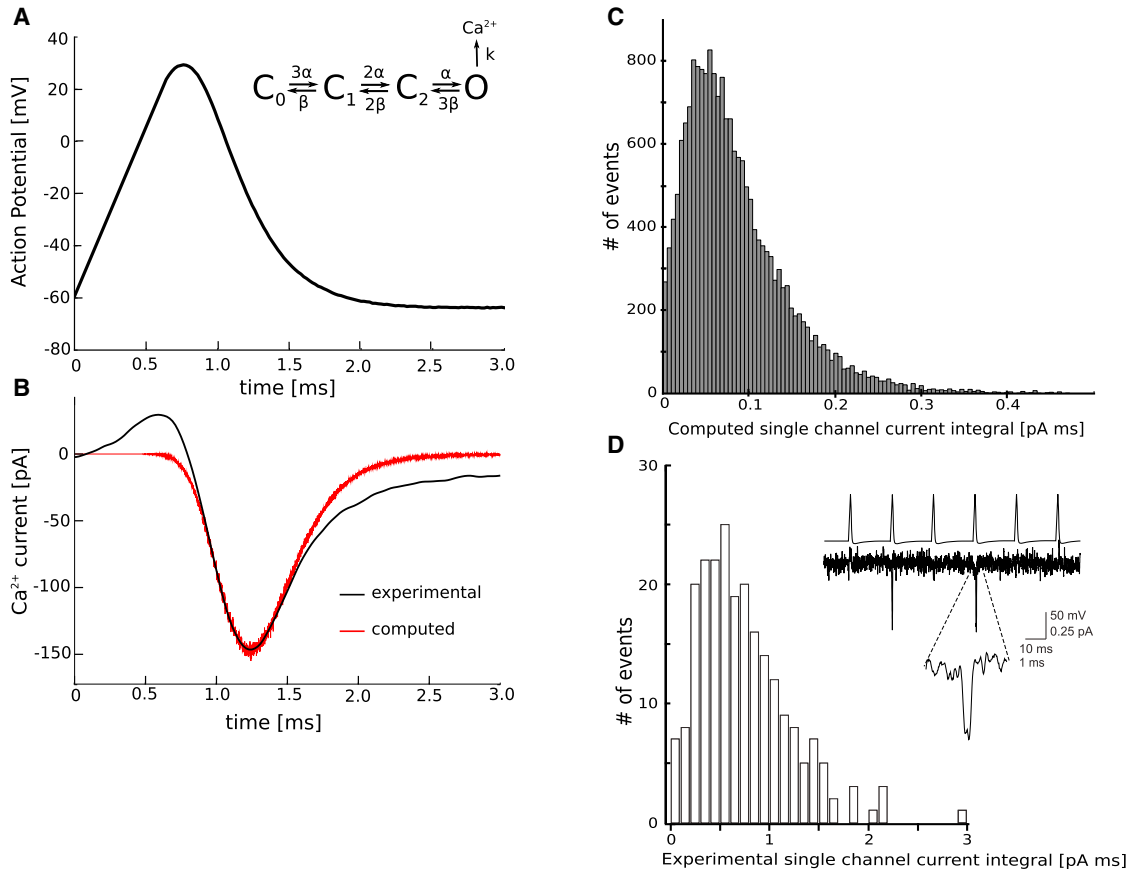

FIGURE 2 Experimental and computed whole-cell and single-channel current integrals. (*A*) The action potential waveform used to drive the voltage-dependent rate constants between closed and open states in our four-state kinetic VGCC model (see *inset*). (*B*) Comparison of the experimental and computed whole-cell Ca^{2+} currents obtained using the action potential and kinetic model shown in panel *A*. Initial deviations were due to nonlinear leak subtraction of the complex action potential waveform used to activate Ca^{2+} current. The slightly slower measured deactivation was due to incompletely clamped long neurites extending on either side of the varicose presynaptic bouton. (*C*) Histogram of the computed single-channel current. (*D*) Corresponding histogram of the experimental single-channel current from cell-attached patch-clamp recordings in the chick ciliary ganglion. Inset: Sample single-channel openings (bottom trace) evoked by action potential waveforms (*top trace*). The experimental single-channel currents are larger than the computed ones due to the presence of a high barium concentration in the patch pipette solution (see Supporting Material) (24).

VGCCs by emitting Ca^{2+} ions at the correct rate from open channels for computational efficiency. VGCCs that opened during a simulation emitted Ca^{2+} ions with Poisson probabilities computed from a time-dependent rate constant:

$$k(t) = -\gamma \frac{G}{2e}(V_m(t) - E_{Ca})$$

Here, $G = 2.4$ pS is the channel conductance (24), e is the elementary charge, and $E_{Ca} = +50$ mV is the Ca^{2+} reversal potential (24,25) that gives rise to the time-dependent driving force $V_m(t) - E_{Ca}$. The prefactor $\gamma = ([Ca^{2+}]_{ext}/2\ \text{mM})$ is a scaling constant accounting for the fact that the channel conductance was determined in 2 mM external Ca^{2+} concentration (24). Similarly to α and β above, k was precomputed, stored in a file, and read by MCell at simulation startup. For example, at physiological $[Ca^{2+}]_{ext}$ of 1.8 mM (26,27) and V_m of −60 mV, open VGCCs emitted ions according to a Poisson process at ~750 ms^{-1}. Thus, during each 10 ns time step, most open channels did not release any Ca^{2+} ions. Only rarely would an open VGCC release a single ion, and events with two or more released ions were even rarer. All of these factors combined provided a detailed and accurate description of the physiological distribution of single-channel current latencies and sizes within our model (see Results).

Ca^{2+} binding to buffer, vesicular sensor sites, and vesicle release

During our simulations, diffusing Ca^{2+} ions could bind to presynaptic Ca^{2+} buffer sites and varying numbers of Ca^{2+}-sensor sites located on the bottom of synaptic vesicles (see Fig. 1, *B* and *C*). Binding occurred with simple on and off kinetics according to

$$\text{buffer}_{\text{unbound}} + Ca^{2+} \leftrightarrow \text{buffer}_{\text{bound}}, \quad \text{and}$$
$$\text{sensor}_{\text{unbound}} + Ca^{2+} \leftrightarrow \text{sensor}_{\text{bound}}$$

with rates taken from the literature (see Table 1 and Results). We tracked the occupancy status of individual sensor sites on all vesicles (including the identity of bound Ca^{2+} ions with regard to the VGCC of origin) and stored the resulting time series. We then analyzed these data postsimulation and extracted the number and timing of vesicle fusion events at a physiological $[Ca^{2+}]_{ext}$ of 1.8 mM (26,27) according to different fusion mechanisms (see Results).

TABLE 1 Summary of model input parameters

Input parameter	Description	References
AZ ultrastructure	Average dimensions of nerve terminal segment, vesicle diameter, location, and number (see Fig. 1).	(17,18)
Diffusion coefficient for free calcium	$D = 6 \times 10^{-6}$ cm^2 s^{-1}	(37,38)
Calcium channel kinetic properties	Three closed states, one open state: $C_0 \leftrightarrow C_1 \leftrightarrow C_2 \leftrightarrow O$; Conductance of open state: 2.4 pS. Voltage-dependent rates of interconversion and Ca^{2+} ion permeation are driven by an action potential waveform. Population kinetics match the whole-cell N-type Ca^{2+} current waveform obtained from cell-attached patch-clamp recordings in the chick ciliary ganglion.	(24) this work
Calcium channel distribution	Two rows of VGCCs run along the membrane depression (13 VGCCs per row, 30 nm from the midline). Channels are spaced regularly in line with the vesicles (one VGCC per vesicle).	(19,30,31)
C2 domain calcium-binding-site properties	Roughly circular layout around the base of each vesicle (see Fig. 1 and Fig. 4, A–D, *insets*); $k_{on} = 1 \times 10^8$ M^{-1}s^{-1}, $k_{off} = 6000$ s^{-1}; mean Ca^{2+} dwell time $= 1/k_{off} = 167$ μs	(7,35)
Calcium buffer binding-site properties	Concentration: 2 mM (~10^6 sites); $k_{on} = 1 \times 10^8$ M^{-1}s^{-1}, $k_{off} = 10000$ s^{-1}; mean Ca^{2+} dwell time $= 1/k_{off} = 100$ μs	(39–43)

Modeling of the single-channel current integral and whole-cell current

We used MCell simulations to generate a histogram of VGCC ion flux and average single-channel current. For this, we employed a simple geometric model consisting of a regular cube of side length 0.2 μm containing a single VGCC (modeled via our four-state kinetic model; see *inset* in Fig. 2 *A*). We then ran 100,000 independent simulations using different random number seeds and recorded the number of released Ca^{2+} ions from which the histogram of single-channel current and average whole-cell current could be computed.

RESULTS

In this section, we describe the development of our excess-Ca^{2+}-binding-site model of neurotransmitter release at the frog NMJ. We begin by outlining the general modeling strategy and then describe in detail the steps that went into model design and validation.

General modeling strategy

Fig. 1 and Table 1 summarize the key components of our model: 1), a spatially realistic AZ geometry of the frog NMJ with docked synaptic vesicles; 2), voltage-gated N-type Ca^{2+} channels (VGCCs); 3), Ca^{2+}-sensor sites at the bottom of synaptic vesicles representing C2 domains of synaptotagmin molecules; and 4), Ca^{2+} buffer sites distributed uniformly and randomly throughout the presynaptic terminal. As will be explained in detail, each of these components was constrained either by experimental data from our laboratory or by established values from the literature.

In each MCell simulation, an action potential triggered stochastic opening and closing of VGCCs located in the presynaptic membrane (see Fig. 1). Open channels gave rise to Ca^{2+} flux into the presynaptic terminal. Ca^{2+} would then diffuse within the AZ, bind to buffer or Ca^{2+}-sensor sites on synaptic vesicles, and eventually leave the AZ. During each simulation run, we tracked all stochastic binding and diffusion events individually. We followed Ca^{2+} ions from individual VGCCs to determine which channels contributed Ca^{2+} to the release of a given synaptic vesicle.

Our model's only unconstrained parameters were the number of Ca^{2+}-sensor sites on synaptic vesicles, n_s, and the fusion mechanism. Here, a fusion mechanism describes how a certain number of Ca^{2+}-sensor sites, n_{sb}, had to be occupied by Ca^{2+} ions for vesicle fusion to occur. Due to the lack of experimental constraints, our fusion mechanism did not include an explicit stochastic step for the actual vesicle fusion event. However, we expect that inclusion of such a step would not change the kinetics and power-law relationships reported in this work. To find viable combinations of numbers of available Ca^{2+}-sensor sites and fusion mechanism, we studied models with varying numbers of sensors, analyzed vesicle fusion for each of a number of different fusion mechanisms, and tested whether our model matched three experimental constraints: 1), the average number of vesicles released per action potential per AZ, n_r; 2), the fourth-order CRR; and 3), the distribution of release latencies. For example, if a particular fusion mechanism required that six of the available Ca^{2+}-binding sites had to be occupied simultaneously by Ca^{2+}, we simply tracked the number of bound ions as a function of time and recorded which vesicles, if any, fulfilled the fusion criterion. To test whether our three experimental constraints were met, we averaged over many trials (typically 10,000) and then determined the average number of released vesicles per AZ and action potential, the distribution of release latencies, and, by varying $[Ca^{2+}]_{ext}$, the CRR. From a simulation-logistics point of view, a change in fusion mechanism only required reanalysis of existing simulation data, whereas changes in simulation parameters (n_s, $[Ca^{2+}]_{ext}$, AZ ultrastructure, etc.) required a completely new set of simulations.

Selection of model parameters

AZ geometry

We chose the frog NMJ as our model system because this preparation has been extensively studied (17,18,28–31). As shown in Fig. S1 *A* in the Supporting Material, the frog NMJ features long and linear synaptic terminals, with regularly spaced AZs running perpendicular to the length of the terminal. Each AZ overlays regularly spaced postsynaptic junctional folds, which are densely packed with acetylcholine receptor proteins. This remarkably organized architecture has allowed direct imaging of multiple AZs within a stimulated nerve terminal, and in particular has enabled high-speed visualization of Ca^{2+} influx with sub-AZ resolution (30).

Our model included a complete frog NMJ AZ (Fig. 1) with dimensions based on published averages (17–19,32). The model's width (1.52 μm) and height (0.945 μm) were taken from typical nerve terminal dimensions, and its length (1.13 μm) was obtained from the average distance between two adjacent Schwann cell invaginations that run between the nerve and muscle cell on either side of an AZ. Because the timescale of a single action potential stimulation event is on the order of milliseconds, the length scale of unbuffered diffusion of Ca^{2+} during this time was on the order of micrometers (computed via $2\sqrt{4D\Delta t/\pi}$; see Table 1 for the value of D). Thus, even in the presence of presynaptic Ca^{2+} buffer, consideration of a full-length AZ was crucial to capture all possible interactions between Ca^{2+} entering through VGCCs positioned near and far from Ca^{2+}-binding sites on individual synaptic vesicles. In our model, a single row of 13 synaptic vesicles was present on each side of a shallow depression representing the membrane region containing double rows of transmembrane particles (up to 200, a fraction of which are thought to represent VGCCs) seen in freeze-fracture electron microscopy images (17,19,33). In a recent study using single-pixel optical fluctuation analysis and MCell simulations (30), we provided strong evidence for an approximate 1:1 ratio of the number of synaptic vesicles and functional VGCCs. Thus, in our model we placed 26 VGCCs on surface mesh tiles in the shallow depression adjacent to the 26 synaptic vesicles, with each vesicle-channel pair separated from one another by a distance of ~35 nm (Fig. 1) (17,19).

VGCC kinetic properties

Our model of neurotransmitter release employs stochastically gated VGCCs driven by a time-dependent action potential waveform. This is in contrast to simpler alternatives used by previous models, such as a constant square wave of Ca^{2+} flux to approximate the average total current during an action potential (4). Although the average total current is clearly an important quantity, our model also captures the underlying complex Ca^{2+} ion conduction dynamics, which may have a significant impact on the timing and sensitivity of vesicle release.

As the action potential invades the AZ within a terminal, only a fraction of functional VGCCs open at all. In a recent study (30), we showed that the opening probability p_o (not to be confused with the often-used probability of being in the open state during a prolonged square wave depolarization) of each individual VGCC during an action potential is low, $p_o \sim 0.2$. Further, even in the rare case when a VGCC does open, the timing of opening and the open duration are stochastic and are driven by voltage- (and thus time-) dependent interconversion rates α and β between open and closed states (see Materials and Methods). Our VGCC kinetic model is depicted schematically in the inset in Fig. 2 *A* and was developed according to the procedure described by DeStefino et al. (34). For our frog AZ model in the absence of any drug treatments, we found that a model with three closed states and a single open state was sufficient to reproduce the rapid activation and deactivation kinetics of the experimental current. Fig. 2 *B* compares an experimentally measured whole-cell current from a large population of VGCCs recorded from a presynaptic varicosity in a frog nerve-muscle coculture ((23) and see Supporting Material) with the average current elicited by our computational model. Both agree well around the peak within the experimental error bars (data not shown). As expected, two aspects of the experimentally measured current were not captured by our modeled current: 1), an initial peak due to nonlinear leak subtraction of the complex action potential waveform used to activate Ca^{2+} current; and 2), slightly slower measured deactivation due to incompletely clamped long neurites extending on either side of the varicose presynaptic bouton. The peak current produced by a population of channels occurred slightly after the peak fraction of open channels, and both occurred 1.1–1.3 ms after the onset of the action potential (data not shown). Further support for the quality of our VGCC model is provided in Fig. 2, *C* and *D*, which show good agreement between experimental single-channel recordings of Ca^{2+} current from chick ciliary ganglion (see also Supporting Material) and corresponding results from MCell simulations using the above four-state model. The opening probability of our VGCCs during an action potential was $p_o \sim 0.2$, in agreement with the value we determined previously (30).

Properties of synaptotagmin C2 domains, Ca^{2+} ions, and Ca^{2+} buffer sites

We placed varying numbers of independent Ca^{2+}-binding sites representing synaptotagmin C2 domains at the bottom of synaptic vesicles resulting in models with 4-, 5-, 6-, 8-, 10-, 20-, 30-, and 40-sensor sites (see Table 2 and *insets* in Fig. 4, *A–C*). The individual binding sites' kinetic Ca^{2+}-binding properties were kept fixed with parameters as summarized in Table 1. The Ca^{2+}-binding ($k_{on,C2} = 1 \times 10^8\ M^{-1}s^{-1}$) and -unbinding ($k_{off,C2} = 6 \times 10^3\ s^{-1}$) rate constants to sensor sites were based on published experimental estimates for synaptotagmin C2A domains (7,35).

TABLE 2 Simulation results for models with varying numbers of sensor sites and fusion mechanisms

n_s	n_{sb}	k_{on} [$M^{-1}s^{-1}$]	n_r	CRR
ind-seq fusion mechanism				
4	4	1.0×10^8	0.16	2.95
4	4	2.5×10^8	1.40	2.64
4	4	4.0×10^8	3.15	2.34
ind-sim fusion mechanism				
4	4	1.0×10^8	0.00	N/A
4	4	2.5×10^8	0.01	N/A
4	4	4.0×10^8	0.02	N/A
5	4	1.0×10^8	0.02	N/A
6	4	1.0×10^8	0.04	N/A
8	4	1.0×10^8	0.14	2.93
10	4	1.0×10^8	0.35	3.36
20	4	1.0×10^8	1.98	3.10
30	4	1.0×10^8	3.98	2.55
40	4	1.0×10^8	5.80	2.23
10	5	1.0×10^8	0.06	4.21
20	**5**	$\mathbf{1.0 \times 10^8}$	**0.78**	**4.12**
30	5	1.0×10^8	2.06	3.46
40	5	1.0×10^8	3.42	3.01
10	6	1.0×10^8	0.01	N/A
20	6	1.0×10^8	0.27	5.71
30	6	1.0×10^8	1.02	4.27
40	6	1.0×10^8	2.00	3.96
10	7	1.0×10^8	0.00	N/A
20	7	1.0×10^8	0.07	N/A
30	7	1.0×10^8	0.47	5.20
40	7	1.0×10^8	1.15	5.07
10	8	1.0×10^8	0.00	N/A
20	8	1.0×10^8	0.02	N/A
30	8	1.0×10^8	0.19	6.89
40	8	1.0×10^8	0.62	5.83
syn-sim fusion mechanism				
20	4	1.0×10^8	0.79	3.65
30	4	1.0×10^8	1.43	3.34
40	4	1.0×10^8	2.03	3.24
20	6	1.0×10^8	0.06	N/A
30	6	1.0×10^8	0.25	5.10
40	**6**	$\mathbf{1.0 \times 10^8}$	**0.49**	**4.65**
20	8	1.0×10^8	0.00	N/A
30	8	1.0×10^8	0.02	N/A
40	8	1.0×10^8	0.08	N/A

This table lists the simulation result for models with increasing numbers of Ca^{2+}-sensor sites on vesicles starting with n_s and $n_{sb} = 4$ using the *ind-seq, ind-sim* and *syn-sim* fusion mechanisms. The two models that match our experimental constraints are highlighted in bold. n_s: total number of available Ca^{2+}-sensor sites on vesicles; n_{sb}: required number of bound Ca^{2+}-sensor sites for vesicle fusion to occur; n_r: number of released vesicles per AZ and action potential.

The chosen value for $k_{on,C2}$ is within the range typically associated with diffusion-limited protein-ligand binding ($k \sim 10^8$–10^{10} $M^{-1}s^{-1}$ (36)), and thus maximizes the sensitivity to diffusing Ca^{2+}. In contrast, $k_{off,C2}$ was moderately fast, resulting in an equilibrium dissociation constant K_D of 60 μM (35), in agreement with experimental measurements and giving rise to a mean occupancy time ($1/k_{off}$) of 167 μs. Our choice of binding parameters provided a good trade-off between sufficient sensitivity toward a very limited supply of diffusing Ca^{2+} ions and sufficiently brief Ca^{2+}-sensor occupancy times to keep the latency distribution narrow.

Because our model contained presynaptic Ca^{2+} buffer sites, the mobility of diffusing Ca^{2+} ions ($D = 6 \times 10^{-6}$ cm^2s^{-1}) was chosen according to freely diffusing Ca^{2+} with a value intermediate between the one determined in neural cytoplasm ($D = 5.3 \times 10^{-6}$ cm^2s^{-1} at room temperature (37)) and neocortex and hippocampus rat brain slices ($D = 7.3 \times 10^{-6}$ cm^2s^{-1} at 23°C (38)). The Ca^{2+} buffer sites bound freely diffusing Ca^{2+} entering the presynaptic space through VGCCs, restricted Ca^{2+} diffusion, and competed with Ca^{2+}-sensor sites on synaptic vesicles for binding of Ca^{2+}. Because reliable estimates of mobile and fixed buffer concentrations in the frog NMJ were not available, we based our estimates on values reported in the crayfish NMJ (39–41). To this end, we added a total concentration of 2 mM static Ca^{2+} buffer to our model, resulting in ~2.3×10^6 discrete buffer sites within the terminal. Buffer sites were placed randomly throughout the terminal and were assumed to represent an upper limit in buffer capacity, encompassing all competing endogenous buffer sources present. The kinetic properties of buffer sites ($k_{on,buff} = 1 \times 10^8$ $M^{-1}s^{-1}$ and $k_{off,buff} = 1 \times 10^4$ s^{-1}) were based on published values (42,43). Although the use of a mixture of static and mobile buffers throughout the terminal might have been more realistic, the resulting increase in computational cost would have been prohibitive. However, at least for small fractions of mobile buffer, we do not expect this approximation to impact our findings qualitatively. For example, simulations using a mixture of 1.9 mM static and 0.1 mM fast mobile buffers ($D = 6 \times 10^{-6}$ $cm^{-2}s^{-1}$) led to a modest 12% reduction in total vesicle release and did not affect the release latency distribution at all.

Determination of experimental constraints for the number of released vesicles, CRR, and fusion latency

We determined the average number of released vesicles per action potential per AZ, n_r, from the average quantal content and count of AZs per terminal (17,18,29). This is illustrated in Fig. S1 *A*, which shows confocal imaging data from our laboratory of the distribution of AZs at the adult frog NMJ. Fig. S1 *B* shows data from two-electrode voltage-clamp recordings of end-plate currents (EPCs) and miniature end-plate currents (mEPCs) in this preparation (see also Supporting Material). Fig. S1 *C* summarizes the counts for the number of AZs and released quanta, leading to an estimate for the number of released vesicles per AZ per action potential of n_r = ~0.5. Thus, vesicle release in each AZ is a rare event and only happens on average with every other action potential stimulus.

To estimate the CRR, we measured the number of release events versus $[Ca^{2+}]_{ext}$ and computed the slope in a log-log

plot. The resulting values for the CRR were in the range of 4–4.2 for the frog NMJ (see Fig. 4, *E* and *F*, and Supporting Material), in agreement with values previously reported in the literature (1). Because experimentally the fourth-order CRR is known to hold at low $[Ca^{2+}]_{ext}$ (<1.0 mM; Fig. 4 *F* (1)), we fitted our MCell simulations over a similar range (0.5–0.9 mM; below 0.5 mM, the number of fusion events even during 10,000 trials was too small for accurate fitting).

The experimentally measured distribution of synaptic release latencies was taken from the literature (44) and is shown as a red curve in Fig. 3. Release happens in a fairly narrow (1–1.5 ms wide) time window with a synaptic delay of ~1 ms. Because we did not know when action potential onset occurred for the data reported in Katz and Miledi (44), for comparison with our simulation data, we could only compare the shapes of the experimental and simulated latency distribution, and not their relative timing.

Determination of the number of Ca^{2+}-binding sites on vesicles and the vesicle fusion mechanism

With the parameters of our AZ model well constrained as described above, we sought to determine viable combinations of numbers of Ca^{2+}-binding sites on synaptic vesicles, n_s, and the fusion mechanism for synaptic vesicle release. (As mentioned above, a fusion mechanism describes the number, manner, and timing with which Ca^{2+} ions have to occupy vesicular sensor sites to trigger release.) To this end, we considered three different fusion mechanisms:

1. *Independent-simultaneous binding (ind-sim)*

Release was triggered by simultaneous Ca^{2+} occupancy of n_{sb} out of the total of n_s-sensor sites on vesicles (the binding events themselves did not have to occur simultaneously). No constraints were imposed on which of the n_s-sensor sites had to bind Ca^{2+}. In other words, fusion occurred as soon as Ca^{2+} occupied n_{sb} sites (see *insets* in Fig. 4, *A* and *B*).

2. *Independent-sequential binding (ind-seq)*

This mechanism was similar to the *ind-sim* mechanism with the exception that not all of the n_{sb} sites had to be occupied by Ca^{2+} simultaneously. Thus, release occurred as soon as the n_{sb}th site bound Ca^{2+} even if a previously occupied site had unbound its Ca^{2+} ion in the meantime.

3. *Synaptotagmin-simultaneous binding (syn-sim)*

This fusion mechanism built on the *ind-sim* mechanism. In addition to simultaneous occupancy of n_{sb} binding sites, Ca^{2+} had to bind to a particular spatial arrangement of sensor sites that are thought to model individual synaptotagmin molecules to trigger fusion (see *insets* of Fig. 4, *C* and *D*).

We then used the Ca^{2+}-binding data obtained from MCell simulations to evaluate each of these fusion mechanisms. For a given fusion mechanism and number of Ca^{2+}-binding sites n_s on vesicles, we calculated the average number of released synaptic vesicles n_r, the latency distribution of release, and the CRR by varying $[Ca^{2+}]_{ext}$.

A model with only a small number of Ca^{2+}-binding sites, $n_s = 4$, does not match our constraints

Based on the approximately fourth-order relationship for the experimentally measured CRR (Fig. 4) (1), a natural choice for the number of sensor sites available and occupied on vesicles was four ($n_s = 4$ and $n_{sb} = 4$). In fact, the presence of four to five cooperative binding sites is the prevailing conceptual view in the literature (1,4,6,45). However, as shown in Table 2, our corresponding model produced too few vesicle release events for both the *ind-seq* ($n_r = 0.16$) and *ind-sim* ($n_r = 0.003$) fusion mechanisms, significantly short of our experimentally measured value of $n_r = 0.5$. Further, as also shown in Table 2, the sensitivity toward increases in $[Ca^{2+}]_{ext}$ was too low, resulting in a CRR that was either

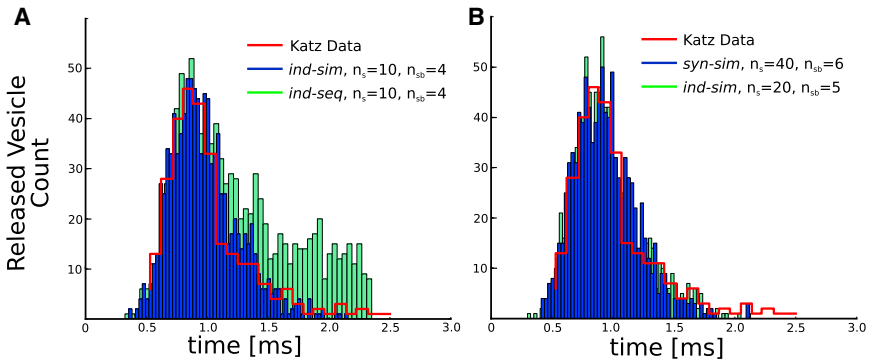

FIGURE 3 Comparison of vesicle-release latencies. (*A*) Histograms of vesicle-release latencies for a model with $n_s = 10$ and $n_{sb} = 4$ for simultaneous (blue, *ind-sim*) and sequential (green, *ind-seq*) fusion mechanisms. For comparison, the red graph depicts the data from Katz and Miledi (44) showing that sequential binding leads to a significantly broadened latency distribution. The sudden cutoff in the histogram of the sequential model at 2.35 ms is an artifact due to the 3 ms simulation window and the fact that the histogram was shifted left to overlap with the Katz data (the actual latency extended well beyond 2.35 ms). (*B*) Latency distribution for $n_s = 20$, $n_{sb} = 5$ with the *ind-sim* fusion mechanism, and $n_s = 40$, $n_{sb} = 6$ with the *syn-sim* mechanism, both of which agree well with the data from Katz and Miledi (44). See Table 2 legend for definition of n_s and n_{sb}.

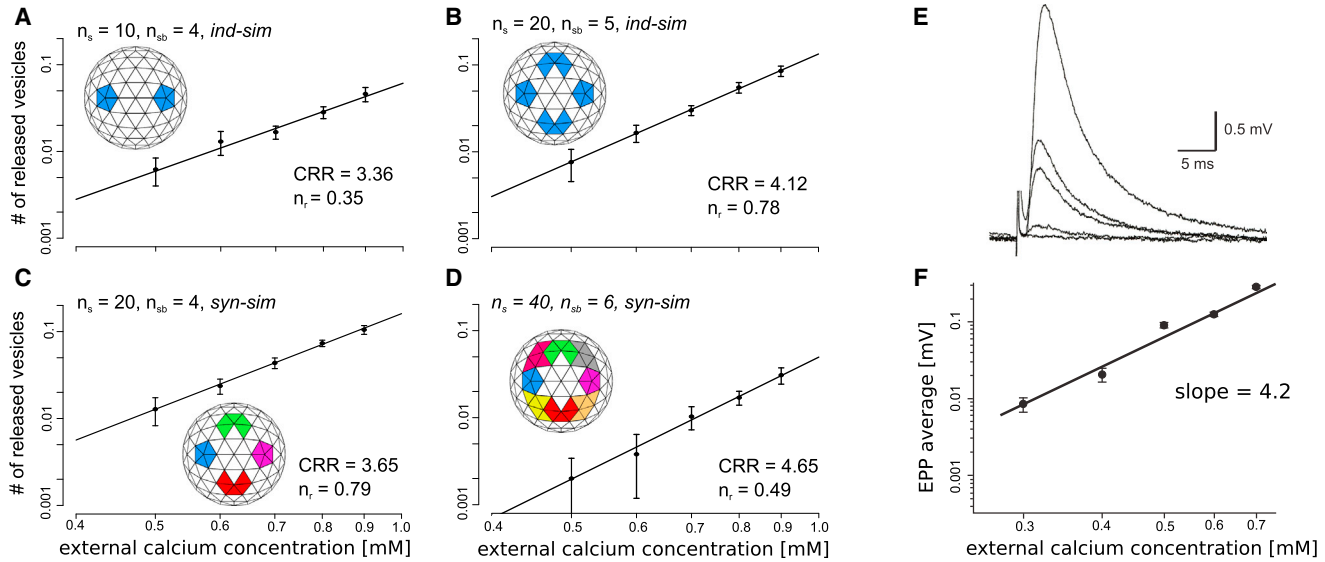

FIGURE 4 Computed and measured CRRs. (*A–D*) Fits for the CRR from simulation data. The inset in each panel shows the arrangement of Ca^{2+}-binding sites on the bottom of synaptic vesicles. (*C* and *D*) For the *syn-sim* fusion mechanism, identically colored regions of five-sensor sites each represent individual synaptotagmin molecules. (*A* and *B*) Results for a 10- and 20-sensor arrangement using the *ind-sim* fusion mechanism. Although the 10-sensor model was not sensitive enough to changes in $[Ca^{2+}]_{ext}$, the 20-sensor model provided a good match with a CRR of 4.12. (*C*) Results for a 20-sensor arrangement, $n_{sb} = 4$, and the *syn-sim* fusion model, which was too insensitive to changes in $[Ca^{2+}]_{ext}$ with a CRR of 3.65. However, as shown in *D*, a further increase in the number of available Ca^{2+}-sensor sites to 40, $n_{sb} = 6$, combined with the *syn-sim* fusion mechanism led to a model that agreed well both in terms of the CRR (4.65) and the number of released vesicles ($n_r = 0.49$). (*E* and *F*) Experimentally measured CRRs. (*E*) Recordings from a representative NMJ (averages of 15 EPPs each recorded at extracellular Ca^{2+} concentrations of 0.3, 0.4, 0.5, 0.6, 0.7 mM Ca^{2+}, in order of increasing peak height). (*F*) Log-log plot and linear regression of the representative data shown in *E*; the slope of this linear regression is 4.2. When examined in 12 NMJs, the average slope of the linear regression was 4.24 ± 0.76 (mean ± SD). See Table 2 legend for definition of n_s, n_{sb}, and n_r.

too small (CRR = 2.95 for *ind-seq* fusion mechanism) or could not be reliably calculated due to the limited number of release events. Although we could further boost the number of released vesicles by increasing the already fast sensor on-rate to $k_{on,C2} = 2.5 \times 10^8\ M^{-1}s^{-1}$ or $k_{on,C2} = 4.0 \times 10^8\ M^{-1}s^{-1}$ (while keeping K_D fixed), this did not in fact increase the CRR. Thus, a model with four independent Ca^{2+}-binding sites on synaptic vesicles was clearly insufficient to model our experimentally observed vesicle release.

Narrow release latency distribution requires simultaneous occupancy of Ca^{2+}-sensor sites at the time of fusion

In Fig. 3 *A* we show the computed latency distribution for both the *ind-seq* and *ind-sim* fusion mechanisms with $n_s = 10$ and $n_{sb} = 4$. A comparison of the modeled distributions with the experimental data reported in Katz and Miledi (44) (*green/blue* versus *red histogram* in Fig. 3 *A*) revealed that the latency distribution for the *ind-seq* mechanism was significantly too broad and extended beyond 2.5 ms in duration compared with the ~1 ms observed experimentally. In contrast, the latency distribution for the *ind-sim* mechanism was much narrower and agreed well with the experimental data. In fact, this finding held true for all fusion mechanisms studied: the focused and narrow latency distribution seen experimentally required the simultaneous occupancy of Ca^{2+} sensors at the time of fusion, and sequential occupancy inevitably led to latency distributions that were much too broad. Thus, we ruled out sequential occupancy as a viable fusion mechanism and henceforth only considered the *ind-sim* and *syn-sim* fusion mechanisms.

Additional Ca^{2+}-sensor sites on vesicles provide increased sensitivity

To increase both the average number of released vesicles, n_r, and the sensitivity toward changes in $[Ca^{2+}]_{ext}$ while keeping the latency distribution narrow and focused, we increased the number of available Ca^{2+}-binding sites on vesicles and required that only a subset of them had to be occupied to trigger release using our *ind-sim* fusion mechanism.

Table 2 lists the number of released vesicles and CRR values for simulation models with increasing numbers of Ca^{2+}-sensor sites (n_s = 5, 6, 8, 10, 20, 30, and 40), only a subset of which had to be occupied simultaneously by Ca^{2+} to trigger release (n_{sb} = 4, 5, 6, 7, and 8) using the *ind-sim* fusion mechanism. These data illustrate an important trend: for a given n_{sb}, as the total number of available sites was increased, the number of released vesicles also increased, whereas the sensitivity toward external Ca^{2+} (CRR) went down.

Given our specific experimental constraints of $n_r = 0.5$ and CRR = 4.2 (Fig. 4), Table 2 suggests that a model

with 20-sensor sites, five of which had to be occupied by Ca^{2+} according to our *ind-sim* mechanism for fusion to take place ($n_s = 20$, $n_{sb} = 5$), provided a close match. The latency distribution of this model was also in good agreement with experimental data as shown in Fig. 3 *B*.

Increasing biochemical realism by modeling distinct synaptotagmin molecules

Based on the good match of the above 20-sensor model combined with the *ind-sim* fusion mechanism, we wondered whether we could incorporate additional structural and biochemical data to further constrain the nature of our model's vesicle release mechanism. Recent studies have provided strong evidence that the Ca^{2+} sensor on synaptic vesicles triggering release is synaptotagmin (9), and that each vesicle may contain seven to eight (10) and up to 15 synaptotagmin molecules (11). Because each synaptotagmin has five Ca^{2+}-binding sites (three on the C2A and two on the C2B domain), we identified groups of five adjacent Ca^{2+}-sensor sites in our model as individual synaptotagmin molecules (see Fig. 1 and *insets* in Fig. 4, *C* and *D*). Further, studies have shown that the C2A and C2B domains each have to bind at least a single Ca^{2+} ion for synaptotagmin to be activated (46). This insight led us to further refine our *ind-sim* fusion mechanism into the *syn-sim* mechanism introduced above. Here, a total of n_s Ca^{2+}-binding sites were subdivided into sets of five corresponding to $n_s/5$ synaptotagmin molecules and their respective five Ca^{2+}-binding sites. To trigger fusion, a given number of synaptotagmin molecules (cassette of five binding sites) had to each be occupied by two Ca^{2+} ions simultaneously. Here, we assumed that the binding of Ca^{2+} to individual synaptotagmin sites in the *syn-sim* fusion mechanism was independent and that each site had the same affinity. This is an approximation, since the K_D values for binding of multiple Ca^{2+} ions to synaptotagmin C2 domains have been shown to be different (47).

In Table 2 we summarize our simulation data for the *syn-sim* mechanism, which followed a trend similar to that observed for the *ind-sim* case: as n_{sb} remained fixed, an increase in n_s also increased n_r and lowered the CRR. Thus, our model revealed that by changing the number of available and occupied Ca^{2+}-binding sites (n_s and n_{sb}), the release machinery could be tuned over a considerable range of n_r and CRR values, thus enabling different types of synapses to adjust their physiological response to Ca^{2+} influx.

Due to the additional constraint of binding to distinct synaptotagmin sites, the *syn-sim* mechanism was less sensitive to Ca^{2+} than the *ind-sim* mechanism. For example, a 20-sensor model combined with simultaneous occupancy of two synaptotagmin molecules by two Ca^{2+} each ($n_{sb} = 4$) agrees with the number of released vesicles per action potential ($n_r = 0.79$) but was not quite sensitive enough to changes in external Ca^{2+} with a CRR of 3.65.

As Table 2 shows, a 40-sensor model that triggered vesicle fusion when three synaptotagmin molecules were each occupied by two Ca^{2+} ions ($n_{sb} = 6$) predicted the experimentally measured number of released vesicles ($n_r = 0.49$) and CRR (4.65) well, even though the latter was perhaps slightly overestimated. Fig. 3 *B* compares the experimentally measured latency distribution with the simulated values for the 40-sensor model, showing excellent agreement. Thus, the 40-sensor model combined with the *syn-sim* fusion mechanism and $n_{sb} = 6$ closely maps to available biochemical data, such as the number of synaptotagmin molecules and available Ca^{2+}-binding sites, while reproducing all of our experimental constraints (i.e., number of released vesicles, latency distribution, and CRR). Although a 20-sensor model combined with the *ind-sim* fusion mechanism also predicted our experimental constraints reasonably well, we prefer the 40-sensor model because it provides a more faithful and realistic representation of available structural and biochemical data as outlined above.

In summary, our model demonstrated that an excess of available Ca^{2+}-sensor sites (20 or 40) of which only a subset had to be occupied by Ca^{2+} to trigger vesicle fusion was necessary to maintain sufficient sensitivity to Ca^{2+} in the presence of competing buffer sites. Furthermore, simultaneous occupancy of sensor sites by Ca^{2+} at the time of release was required to keep the release latency distribution sufficiently narrow.

The Ca^{2+} concentration in the vicinity of sensor sites on vesicles is very low

With our newly developed excess-Ca^{2+}-binding-site model in hand, we could take a closer look at the distribution of Ca^{2+} within the terminal and in particular the concentration of free Ca^{2+} ions in the vicinity of the sensor sites on the bottom of synaptic vesicles. To this end, we added sampling boxes below each synaptic vesicle, which were transparent to Ca^{2+} ions and thus did not impede free Ca^{2+} diffusion. The Ca^{2+}-accessible volume of the subvesicular sampling boxes was ~15,750 nm^3. Fig. 5 shows the average number and concentration of free Ca^{2+} ions below released synaptic vesicles as a function of time (averaged over ~4900 release events). Clearly, at any given instance, the number of free Ca^{2+} ions that were below vesicles and thus available for binding to synaptotagmin was very small. Although the peak concentration reached micromolar values over the course of a single action potential, during any given simulation time step (dt = 10 ns) there was typically no (or at most a single) Ca^{2+} ion present in the small space between the bottom of a synaptic vesicle and the presynaptic membrane (leading to an average number of ions well below one). This extremely limited nature of freely diffusing Ca^{2+} ions in the vicinity of synaptic vesicles explains the observed need for an excess of Ca^{2+}-binding sites.

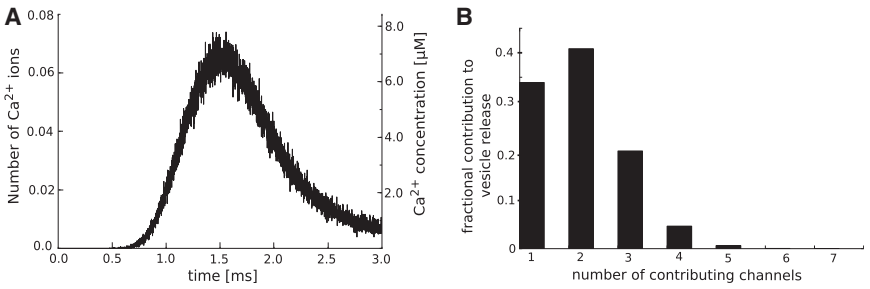

FIGURE 5 Subvesicular Ca^{2+} concentration and VGCC contribution to release. (*A*) Average number and concentration of free Ca^{2+} in the confined space just below released synaptic vesicles (close to Ca^{2+}-sensor sites, average over ~4900 release events). Although the Ca^{2+} concentration can reach micromolar values, the average number of discrete Ca^{2+} that are present at any given point in time is very small. This emphasizes the extreme sparseness of free Ca^{2+} and thus the need for an excess of available Ca^{2+}-binding sites on synaptic vesicles to achieve experimentally measured rates of release and CRR. (*B*) Fractional contribution of increasing numbers of VGCCs to the release of individual synaptic vesicles. The large majority of release events are triggered by Ca^{2+} ions from one or two Ca^{2+} channels, highlighting the highly localized (nanodomain (48)) coupling of VGCCs to synaptic vesicles.

Vesicle release is overwhelmingly triggered by nearby Ca^{2+} channels

The particle-based nature of our MCell simulations allowed us to track Ca^{2+} ions emerging from individual open VGCCs and thus determine the contribution of individual Ca^{2+} channels to the release of synaptic vesicles. Fig. 5 *B* shows the fractional contribution of different numbers of Ca^{2+} channels to the release of individual vesicles. The large majority of release events (~75%) were triggered by Ca^{2+} ions from a single Ca^{2+} channel (34%) or two channels (41%), followed by a 20% contribution from three channels. Vesicle release events triggered by Ca^{2+} ions from more than three channels were extremely rare. Overall, the average number of channels contributing Ca^{2+} to the release of a single vesicle (channel cooperativity) was 1.97, in agreement with the value of 1.7 reported in Shahrezaei et al. (4). Thus, our model highlights the extremely localized nature of the cloud of Ca^{2+} ions involved in the release of a vesicle. Ca^{2+} ions that contributed to release emanated from Ca^{2+} channels in the close vicinity of a vesicle (nanodomain coupling (48)).

DISCUSSION

The vertebrate NMJ is optimized for high-fidelity transmission of electrical activity between nerve and muscle cells. Each nerve action potential must produce a corresponding muscle contraction with a short and reliable synaptic latency. It follows that neurotransmitter release from synaptic vesicles has to occur with similar precision. Defects in vesicle release or postsynaptic response lead to an increase in the distribution of latencies, which can be detected clinically as increased synaptic jitter by single-fiber electromyography (49).

A relatively small number of Ca^{2+} ions enter the AZ during each action potential for which binding sites on synaptic vesicles must compete with Ca^{2+} buffer sites. Therefore, the molecular machinery for triggering exocytosis must be exquisitely sensitive to Ca^{2+} and at the same time be able to activate and deactivate very quickly to allow for reliable release during high-frequency stimulation. In addition, the mechanism must allow for reliable modulation of the release probability, which varies considerably among different synapses and within the same synapse as plastic changes occur (50). The critical physiological factors sensitivity, synchrony, and plasticity dictate the biophysical mechanism of Ca^{2+}-dependent transmitter release. In this study, we focused primarily on sensitivity and synchrony at the synapse. The impact of plasticity on our model will be the subject of a future study.

By combining physiological data with quantitative computer simulations, we were able to develop a spatially realistic model of an entire frog AZ. We then used Monte Carlo simulations of our model to predict the Ca^{2+}-binding stoichiometry and dynamics that underlie neurotransmitter release. Our simulations predict a large number of Ca^{2+}-binding sites (up to 40) on each synaptic vesicle. Fusion was triggered when a subset of these sites (typically five to six, depending on the fusion mechanism) was occupied by Ca^{2+} ions. In fact, a model with eight synaptotagmin molecules (corresponding to 40 Ca^{2+}-binding sites), three of which each had to simultaneously be occupied by two Ca^{2+} ions to trigger vesicle fusion, satisfied all of our experimental constraints, i.e., the average number of vesicles released per action potential per AZ, the fourth-order dependence of release on the extracellular Ca^{2+} concentration, CRR, and the distribution of release latencies. Our predicted number of binding sites agrees with published experimental estimates of the number of available SNARE complexes within a fusion pore (13) and synaptotagmin molecules per synaptic vesicle (10,11). Although Takamori et al. (11) estimated that up to 15 synaptotagmin molecules are present on synaptic vesicles, these molecules may be distributed over both vesicle hemispheres and thus may not all participate functionally in the spatially localized fusion machinery at the presynaptic membrane. Similar to other components of our model, the predicted number of synaptotagmin molecules represents an average value per vesicle. It will be interesting to explore the impact of variability in the number of synaptotagmin molecules per vesicle within the framework of our model in future work.

Particle-based Monte Carlo simulations provide crucial microscopic insight

Earlier studies of synaptic function used various combinations of deterministic (6,8,39) and Monte Carlo methods (4,51,52). Because the absolute amount of Ca^{2+} ions is in such limited supply (see Results, in particular Fig. 5 *A*), accurate stochastic modeling of Ca^{2+} influx via particle-based Monte Carlo methods combined with a spatially realistic AZ geometry is crucial for capturing the underlying Ca^{2+}-binding dynamics. Using MCell, we were able to track diffusing Ca^{2+} ions and thereby determine the VGCC of origin for ions that bound to vesicles and contributed to synaptic vesicle fusion. Our data showed that vesicle release at the frog NMJ is triggered by a highly localized cloud (nanodomain) of Ca^{2+} ions predominantly contributed by the channel closest to the released vesicle, assisted by a small number of Ca^{2+} ions from one or at most two additional channels located slightly farther away. This agrees well with experimental and simulation data from chick ciliary ganglion synapses (53), frog NMJ (4), basket cell-granule cell synapses (54), and excitatory CA3-CA1 synapses (55), where it also appears that small numbers of Ca^{2+} channels can trigger release of synaptic vesicles. Thus, each vesicle and its closely associated Ca^{2+} channel act as an independent unit, a single-vesicle release site. It then follows that the properties of a complete AZ can be approximated as the independent sum of these single-vesicle release sites (48).

Excess Ca^{2+}-binding sites without any classical binding-site cooperativity can explain the observed Ca^{2+}-release relationship

The apparent fourth-order relationship between extracellular Ca^{2+} concentration and neurotransmitter release was first attributed to classical cooperativity between Ca^{2+}-binding sites (1). Our MCell simulations reproduced the fourth-order CRR in the presence of independent Ca^{2+}-sensor sites on synaptic vesicles with constant on and off rates, suggesting that classical cooperativity related to binding of Ca^{2+} is not required. Instead, the availability of excess Ca^{2+}-binding sites is sufficient to reproduce the experimentally measured fourth-order CRR.

Other forms of cooperativity related to fusion can be envisioned. Recent experimental data (46) suggest that two binding sites on a single synaptotagmin molecule (C2A and C2B) may need to become occupied before they contribute to fusion, and we successfully modeled this scenario with our *syn-sim* fusion mechanism. Both our *syn-sim* and *ind-sim* mechanisms are equally plausible based on our results, and both are consistent with fusion mediated by three to eight synaptotagmin-activated SNARE complexes arrayed around a docked synaptic vesicle (9,13).

CONCLUSIONS

We have developed a comprehensive and predictive model of action-potential-triggered fusion of synaptic vesicles at the frog NMJ. Our model reconciles recent biochemical findings on the characteristics of the Ca^{2+} sensors on synaptic vesicles (synaptotagmin molecules with five Ca^{2+}-binding sites each) with extensive physiology data, including the number of released vesicles, the release latency distribution, and the fourth-order CRR. Our stochastic Monte Carlo simulations reveal that the design of the AZ and in particular that of the vesicle release apparatus are fundamentally driven by the extremely limited and localized nature of Ca^{2+} ions after an action potential invades the presynaptic space and VGCCs open stochastically. This in turn requires an excess of Ca^{2+}-binding sites in the form of up to eight synaptotagmin molecules at the bottom of each synaptic vesicle to ensure the sensitivity and synchrony of the system. In the future, we will extend our approach to investigate synaptic plasticity and AZ structure/function relationships at mammalian NMJs.

SUPPORTING MATERIAL

Supporting experimental procedures, one figure, and references (56–58) are available at http://www.biophysj.org/biophysj/supplemental/S0006-3495(13)00579-1.

We thank J. Czech for help with creating some of the images.

This work was supported by grants from the National Institutes of Health (P41RR06009 and P41GM103712 to M.D.), and the National Science Foundation (0844174 to M.D., 0844604 to S.D.M., and 1249546 to M.D. and S.D.M.).

REFERENCES

1. Dodge, Jr., F. A., and R. Rahamimoff. 1967. Co-operative action a calcium ions in transmitter release at the neuromuscular junction. *J. Physiol.* 193:419–432.
2. Schneggenburger, R., and E. Neher. 2000. Intracellular calcium dependence of transmitter release rates at a fast central synapse. *Nature.* 406:889–893.
3. Bennett, M. R., L. Farnell, and W. G. Gibson. 2000. The probability of quantal secretion near a single calcium channel of an active zone. *Biophys. J.* 78:2201–2221.
4. Shahrezaei, V., A. Cao, and K. R. Delaney. 2006. Ca^{2+} from one or two channels controls fusion of a single vesicle at the frog neuromuscular junction. *J. Neurosci.* 26:13240–13249.
5. Bollmann, J. H., and B. Sakmann. 2005. Control of synaptic strength and timing by the release-site Ca^{2+} signal. *Nat. Neurosci.* 8:426–434.
6. Matveev, V., R. Bertram, and A. Sherman. 2006. Residual bound Ca^{2+} can account for the effects of Ca^{2+} buffers on synaptic facilitation. *J. Neurophysiol.* 96:3389–3397.
7. Millar, A. G., R. S. Zucker, …, H. L. Atwood. 2005. Calcium sensitivity of neurotransmitter release differs at phasic and tonic synapses. *J. Neurosci.* 25:3113–3125.
8. Pan, B., and R. S. Zucker. 2009. A general model of synaptic transmission and short-term plasticity. *Neuron.* 62:539–554.
9. Chapman, E. R. 2002. Synaptotagmin: a Ca^{2+} sensor that triggers exocytosis? *Nat. Rev. Mol. Cell Biol.* 3:498–508.

10. Mutch, S. A., P. Kensel-Hammes, …, D. T. Chiu. 2011. Protein quantification at the single vesicle level reveals that a subset of synaptic vesicle proteins are trafficked with high precision. *J. Neurosci.* 31:1461–1470.

11. Takamori, S., M. Holt, …, R. Jahn. 2006. Molecular anatomy of a trafficking organelle. *Cell.* 127:831–846.

12. Paddock, B. E., Z. Wang, …, N. E. Reist. 2011. Membrane penetration by synaptotagmin is required for coupling calcium binding to vesicle fusion in vivo. *J. Neurosci.* 31:2248–2257.

13. Han, X., C. T. Wang, …, M. B. Jackson. 2004. Transmembrane segments of syntaxin line the fusion pore of Ca^{2+}-triggered exocytosis. *Science.* 304:289–292.

14. Coggan, J. S., T. M. Bartol, …, T. J. Sejnowski. 2005. Evidence for ectopic neurotransmission at a neuronal synapse. *Science.* 309:446–451.

15. Czech, J., M. Dittrich, and J. R. Stiles. 2009. Rapid creation, Monte Carlo simulation, and visualization of realistic 3D cell models. *In* Methods in Molecular Biology, Systems Biology. I. V. Maly, editor. Humana Press, New York. 237–287.

16. Blender. 2013. Blender 3D creation software, http://www.blender.org/ Accessed: May 1, 2013.

17. Heuser, J. E., T. S. Reese, …, L. Evans. 1979. Synaptic vesicle exocytosis captured by quick freezing and correlated with quantal transmitter release. *J. Cell Biol.* 81:275–300.

18. Pawson, P. A., A. D. Grinnell, and B. Wolowske. 1998. Quantitative freeze-fracture analysis of the frog neuromuscular junction synapse—I. Naturally occurring variability in active zone structure. *J. Neurocytol.* 27:361–377.

19. Stanley, E. F., T. S. Reese, and G. Z. Wang. 2003. Molecular scaffold reorganization at the transmitter release site with vesicle exocytosis or botulinum toxin C1. *Eur. J. Neurosci.* 18:2403–2407.

20. Stiles, J. R., and T. M. Bartol. 2001. Monte Carlo methods for simulating realistic synaptic microphysiology using MCell. *In* Computational Neuroscience: Realistic Modeling For Experimentalists. E. De Schutter, editor. CRC Press, Boca Raton, FL. 87–127.

21. Kerr, R. A., T. M. Bartol, …, J. R. Stiles. 2008. Fast Monte Carlo simulation methods for biological reaction-diffusion systems in solution and on surfaces. *SIAM J. Sci. Comput.* 30:3126–3149.

22. Stiles, J. R., T. M. Bartol, …, T. J. Sejnowski. 2001. Synaptic variability: new insights from reconstructions and Monte Carlo simulations with MCell. *Synapses.* 1:681–731.

23. Pattillo, J. M., B. Yazejian, …, S. D. Meriney. 2001. Contribution of presynaptic calcium-activated potassium currents to transmitter release regulation in cultured Xenopus nerve-muscle synapses. *Neuroscience.* 102:229–240.

24. Church, P. J., and E. F. Stanley. 1996. Single L-type calcium channel conductance with physiological levels of calcium in chick ciliary ganglion neurons. *J. Physiol.* 496:59–68.

25. Campbell, D. L., W. R. Giles, …, E. F. Shibata. 1988. Reversal potential of the calcium current in bull-frog atrial myocytes. *J. Physiol.* 403:267–286.

26. Del Castillo, J., and L. Stark. 1952. The effect of calcium ions on the motor end-plate potentials. *J. Physiol.* 116:507–515.

27. Del Castillo, J., and B. Katz. 1954. Quantal components of the end-plate potential. *J. Physiol.* 124:560–573.

28. Katz, B., and R. Miledi. 1965. The effect of calcium on acetylcholine release from motor nerve terminals. *Proc. R. Soc. Lond. B Biol. Sci.* 116:496–503.

29. Katz, B., and R. Miledi. 1979. Estimates of quantal content during 'chemical potentiation' of transmitter release. *Proc. R. Soc. Lond. B Biol. Sci.* 205:369–378.

30. Luo, F., M. Dittrich, …, S. D. Meriney. 2011. Single-pixel optical fluctuation analysis of calcium channel function in active zones of motor nerve terminals. *J. Neurosci.* 31:11268–11281.

31. Wachman, E. S., R. E. Poage, …, S. D. Meriney. 2004. Spatial distribution of calcium entry evoked by single action potentials within the presynaptic active zone. *J. Neurosci.* 24:2877–2885.

32. Bennett, M. R., L. Farnell, and W. G. Gibson. 2000. The probability of quantal secretion within an array of calcium channels of an active zone. *Biophys. J.* 78:2222–2240.

33. Pumplin, D. W., T. S. Reese, and R. Llinás. 1981. Are the presynaptic membrane particles the calcium channels? *Proc. Natl. Acad. Sci. USA.* 78:7210–7213.

34. DeStefino, N. R., A. A. Pilato, …, S. D. Meriney. 2010. (R)-roscovitine prolongs the mean open time of unitary N-type calcium channel currents. *Neuroscience.* 167:838–849.

35. Davis, A. F., J. Bai, …, E. R. Chapman. 1999. Kinetics of synaptotagmin responses to Ca^{2+} and assembly with the core SNARE complex onto membranes. *Neuron.* 24:363–376.

36. Alberty, R. A., and G. G. Hammes. 1958. Application of the theory of diffusion-controlled reactions to enzyme kinetics. *J. Phys. Chem.* 62:154–159.

37. Donahue, B. S., and R. F. Abercrombie. 1987. Free diffusion coefficient of ionic calcium in cytoplasm. *Cell Calcium.* 8:437–448.

38. Hrabetová, S., D. Masri, …, C. Nicholson. 2009. Calcium diffusion enhanced after cleavage of negatively charged components of brain extracellular matrix by chondroitinase ABC. *J. Physiol.* 587:4029–4049.

39. Matveev, V., A. Sherman, and R. S. Zucker. 2002. New and corrected simulations of synaptic facilitation. *Biophys. J.* 83:1368–1373.

40. Matveev, V., R. S. Zucker, and A. Sherman. 2004. Facilitation through buffer saturation: constraints on endogenous buffering properties. *Biophys. J.* 86:2691–2709.

41. Gilmanov, I. R., D. V. Samigullin, …, E. A. Bukharaeva. 2008. Modeling of quantal neurotransmitter release kinetics in the presence of fixed and mobile calcium buffers. *J. Comput. Neurosci.* 25:296–307.

42. Xu, T., M. Naraghi, …, E. Neher. 1997. Kinetic studies of Ca^{2+} binding and Ca^{2+} clearance in the cytosol of adrenal chromaffin cells. *Biophys. J.* 73:532–545.

43. Yazejian, B., X. P. Sun, and A. D. Grinnell. 2000. Tracking presynaptic Ca^{2+} dynamics during neurotransmitter release with Ca^{2+}-activated K^+ channels. *Nat. Neurosci.* 3:566–571.

44. Katz, B., and R. Miledi. 1965. The measurement of synaptic delay, and the time course of acetylcholine release at the neuromuscular junction. *Proc. R. Soc. Lond. B Biol. Sci.* 161:483–495.

45. Shahrezaei, V., and K. R. Delaney. 2004. Consequences of molecular-level Ca^{2+} channel and synaptic vesicle colocalization for the Ca^{2+} microdomain and neurotransmitter exocytosis: a Monte Carlo study. *Biophys. J.* 87:2352–2364.

46. Earles, C. A., J. Bai, …, E. R. Chapman. 2001. The tandem C2 domains of synaptotagmin contain redundant Ca2+ binding sites that cooperate to engage t-SNAREs and trigger exocytosis. *J. Cell Biol.* 154:1117–1123.

47. Ubach, J., X. Zhang, …, J. Rizo. 1998. Ca^{2+} binding to synaptotagmin: how many Ca^{2+} ions bind to the tip of a C_2-domain? *EMBO J.* 17:3921–3930.

48. Tarr, T. B., M. Dittrich, and S. D. Meriney. 2013. Are unreliable release mechanisms conserved from NMJ to CNS? *Trends Neurosci.* 36:14–22.

49. Stålberg, E., and J. V. Trontelj. 1979. Single Fibre Electromyography. Mirvalle Press, Old Woking, Surrey, UK.

50. Schneggenburger, R., and E. Neher. 2005. Presynaptic calcium and control of vesicle fusion. *Curr. Opin. Neurobiol.* 15:266–274.

51. Kennedy, K. M., S. T. Piper, and H. L. Atwood. 1999. Synaptic vesicle recruitment for release explored by Monte Carlo stimulation at the crayfish neuromuscular junction. *Can. J. Physiol. Pharmacol.* 77:634–650.

52. Glavinović, M. I., and H. R. Rabie. 2001. Monte Carlo evaluation of quantal analysis in the light of Ca^{2+} dynamics and the geometry of secretion. *Pflugers Arch.* 443:132–145.

53. Stanley, E. F. 1993. Single calcium channels and acetylcholine release at a presynaptic nerve terminal. *Neuron.* 11:1007–1011.

54. Bucurenciu, I., J. Bischofberger, and P. Jonas. 2010. A small number of open Ca^{2+} channels trigger transmitter release at a central GABAergic synapse. *Nat. Neurosci.* 13:19–21.

55. Scimemi, A., and J. S. Diamond. 2012. The number and organization of Ca^{2+} channels in the active zone shapes neurotransmitter release from Schaffer collateral synapses. *J. Neurosci.* 32:18157–18176.

56. Hamburger, V., and H. L. Hamilton. 1951. A series of normal stages in the development of the chick embryo. *J. Morphol.* 88:49–92.

57. White, M. G., M. A. Crumling, and S. D. Meriney. 1997. Developmental changes in calcium current pharmacology and somatostatin inhibition in chick parasympathetic neurons. *J. Neurosci.* 17:6302–6313.

58. Cho, S., and S. D. Meriney. 2006. The effects of presynaptic calcium channel modulation by roscovitine on transmitter release at the adult frog neuromuscular junction. *Eur. J. Neurosci.* 23:3200–3208.